

---

# TabPFN Extensions for Interpretable Geotechnical Modelling

---

Taiga Saito<sup>a</sup>, Yu Otake<sup>a</sup>, Daijiro Mizutani<sup>a</sup>, Stephen Wu<sup>b,c</sup>

<sup>a</sup>Department of Civil and Environmental Engineering, Tohoku University,  
6-6-06 Aramaki Aoba, Aoba-ku, Sendai, Miyagi 980-8579, Japan

<sup>b</sup>Research Organization of Information and Systems, The Institute of Statistical Mathematics  
10-3 Midori-cho, Tachikawa, Tokyo 190-8562, Japan

<sup>c</sup>Department of Statistical Science, The Graduate University for Advanced Studies  
10-3 Midori-cho, Tachikawa, Tokyo 190-8562, Japan

taiga.saito.r3@dc.tohoku.ac.jp

## Abstract

Geotechnical site characterisation relies on sparse, heterogeneous borehole data where uncertainty quantification and model interpretability are as critical as predictive accuracy for reliable engineering decisions. This paper presents an exploratory investigation into the use of TabPFN [4]—a transformer-based tabular foundation model using in-context learning—and its extension library `tabPFN-extensions` [10] for two geotechnical inference tasks: (1) soil-type classification using N-value and shear-wave velocity data from a synthetic geotechnical dataset, and (2) iterative imputation of five missing mechanical parameters ( $s_u$ ,  $E_u$ ,  $\sigma'_p$ ,  $C_c$ ,  $C_v$ ) in benchmark problem BM/AirportSoilProperties/2/2025 [7]. We apply cosine-similarity analysis to TabPFN-derived embeddings, visualise full posterior distributions from an iterative inference procedure, and compute SHAP-based feature importance—all without model retraining. Learned embeddings clearly separate Clay and Sand samples without explicit soil-type supervision; iterative imputation improves predictions for four of five target parameters, with posterior widths that reflect physically reasonable parameter-specific uncertainty; and SHAP analysis reveals the inter-parameter dependency structure, recovering established geotechnical relationships including the Skempton compression index correlation and the inverse dependence of preconsolidation pressure on water content. These results suggest the potential of foundation-model-based tools to support interpretable, uncertainty-aware parameter inference in data-scarce geotechnical practice.

**Keywords:** TabPFN; geotechnical site characterisation; in-context learning; uncertainty quantification; SHAP

## 1 Introduction

Geotechnical site characterisation is inherently challenged by the scarcity and heterogeneity of borehole measurement data. Reliable prediction of soil mechanical properties—undrained shear strength ( $s_u$ , from unconfined compression test), undrained secant modulus ( $E_u$ ), preconsolidation stress ( $\sigma'_p$ ), compression index ( $C_c$ ), and coefficient of consolidation ( $C_v$ )—is essential for foundation design, liquefaction assessment, and ground improvement planning, yet field data often consist of only tens to hundreds of samples. In engineering applications, the objective extends beyond predictive accuracy: model predictions—particularly for safety-critical decisions such as foundation design—

must be supported by interpretable justification consistent with established physical understanding, and prediction uncertainty must be quantified to enable reliability-based assessments. Consequently, purely black-box approaches that offer high accuracy without interpretability remain difficult to adopt in geotechnical practice.

In geotechnical engineering, parameter inference has traditionally relied on empirical correlations and regression models derived from laboratory and field observations. More recently, probabilistic and Bayesian approaches have been proposed to quantify uncertainty in geotechnical parameters and to leverage data from multiple sites. For example, hierarchical Bayesian models have been developed for constructing quasi-site-specific multivariate probability distributions [3, 17], and similarity-based site retrieval methods have been proposed using Bayesian measures [14, 15]. Data-driven approaches—including dictionary learning for transformation models [2], clustering-based regionalisation [1], and high-order dependence modelling [13]—have further expanded the methodological toolkit for site characterisation. Phoon et al. [8] provided a comprehensive review of the challenges inherent in data-driven site characterisation, and Phoon et al. [9] framed the problem of quantifying site uniqueness as a “facial recognition” challenge for geotechnical data. Despite these advances, the integration of predictive accuracy, interpretability, and uncertainty quantification within a single, easy-to-deploy framework remains an open challenge.

The emergence of foundation models has opened new possibilities for inference in engineering problems. These models can be viewed as a generalisation of conventional statistical inference approaches: rather than training a task-specific model from scratch, a foundation model acquires broad predictive capabilities from large-scale pretraining and adapts to new tasks through in-context learning, providing flexible predictions without extensive model training or hyperparameter tuning. TabPFN [4] is a transformer-based tabular foundation model trained via meta-learning on prior data synthesised from a diverse set of causal relationships commonly observed in tabular data. It performs in-context learning: given a small observed dataset at inference time, the model conditions its predictions on the entire context without gradient-based fine-tuning. Throughout this paper, *training data* refers to the observed samples provided as context to TabPFN at inference time—not data used to update model parameters—and *test data* denotes the samples for which predictions are sought. In a companion study [12], we demonstrated that TabPFN achieves competitive predictive accuracy for geotechnical site characterisation on the BM/AirportSoilProperties benchmark, rivalling conventional regression approaches even under severely limited training data. The `tabpfn-extensions` library [10] further exposes the model’s internal representations, providing access to learned embeddings and SHAP-based feature attribution without any model retraining. The base TabPFN model itself natively outputs full posterior distributions over predictions, which we exploit for iterative inference and uncertainty quantification.

From this perspective, the present paper adopts the generic extension tools of TabPFN [4, 10] for the specific task of site characterisation in order to perform exploratory analyses and to investigate how foundation-model-based approaches may support interpretable parameter inference in geotechnical engineering. Rather than proposing a new algorithm, this study examines the potential of applying an existing foundation model framework to geotechnical problems, with emphasis on interpretability and uncertainty quantification. Specifically, we address three aspects:

1. We apply embedding-based cosine-similarity analysis to a geotechnical soil classification problem, demonstrating that the model’s internal representations capture meaningful soil-type structure without explicit supervision.
2. We perform iterative imputation of missing mechanical parameters and visualise full posterior distributions, providing sample-level uncertainty estimates suitable for reliability-based geotechnical design.
3. We compute SHAP-based feature importance, revealing a physically interpretable two-regime structure in which index properties dominate consolidation parameters while cross-parameter influence governs strength and stiffness predictions.

## 2 Classification Problem: Embedding-Based Similarity Analysis

Site similarity quantification is central to geotechnical site characterisation [14, 15]. This section demonstrates that TabPFN embeddings—extracted as a byproduct of inference—provide a direct,

interpretable measure of sample-level similarity, enabling coverage assessment beyond classification accuracy.

## 2.1 Dataset and Setup

We use a synthetic geotechnical dataset consisting of borehole samples labelled as Clay or Sand. Input features are the standard penetration test N-value and shear-wave velocity  $V_s$ . The dataset is synthetic in the sense that  $V_s$  values were not independently measured but derived from borehole N-values via the empirical formulae  $V_s = 100N^{1/3}$  (Clay) and  $V_s = 80N^{1/3}$  (Sand) prescribed in the Japanese railway seismic design standard [11], making  $V_s$  a deterministic function of  $N$  for each soil class. Because  $V_s$  is uniquely determined by  $(N, \text{soil class})$ , the two classes are perfectly separable in the  $(N, V_s)$  space, making the classification task itself straightforward; the primary purpose of this section is therefore to illustrate the interpretability of TabPFN’s learned embeddings and predicted probability surfaces, rather than to benchmark classification accuracy. The dataset was split into training and test sets; the training set was used to condition TabPFN’s in-context predictions, and the test set was held out for evaluation. The dataset comprises 32 samples in total, randomly split equally into 16 training samples (11 Clay, 5 Sand) and 16 test samples (7 Clay, 9 Sand) (Table 1). This sample size is consistent with the small-data regime typical of geotechnical site investigations, where borehole costs limit the available data to a few tens of samples. Notably, the training set contains only five Sand samples, all with  $N \geq 29$ , whereas the test set includes Sand samples at  $N$  as low as 14—a region not covered by any Sand training sample. Combined with the 11:5 Clay-to-Sand imbalance, this configuration provides a challenging inference scenario in which the model must extrapolate beyond the observed Sand training distribution. As shown in Figure 1, the two soil classes are well-separated in the  $N$ – $V_s$  space, confirming that the joint  $(N, V_s)$  signal serves as an effective soil-type discriminator.

Table 1: All samples in the synthetic geotechnical dataset. No. corresponds to the axis labels in Figure 3: training samples are ordered along the row axis and test samples along the column axis (Clay first, sorted by ascending  $N$ -value; Sand second, sorted by ascending  $N$ -value).

Training set ( $n = 16$ )				Test set ( $n = 16$ )			
No.	$N$	$V_s$ (m/s)	Soil	No.	$N$	$V_s$ (m/s)	Soil
1	1	100.000	Clay	1	4	158.740	Clay
2	2	125.992	Clay	2	5	170.998	Clay
3	7	191.293	Clay	3	9	208.008	Clay
4	12	228.943	Clay	4	10	215.443	Clay
5	15	246.621	Clay	5	11	222.398	Clay
6	16	251.984	Clay	6	28	303.659	Clay
7	17	257.128	Clay	7	38	336.198	Clay
8	18	262.074	Clay	8	14	192.811	Sand
9	20	271.442	Clay	9	25	233.921	Sand
10	27	300.000	Clay	10	27	240.000	Sand
11	29	307.232	Clay	11	30	248.579	Sand
12	29	245.785	Sand	12	33	256.603	Sand
13	42	278.082	Sand	13	38	268.958	Sand
14	43	280.272	Sand	14	40	273.596	Sand
15	47	288.706	Sand	15	45	284.551	Sand
16	48	290.739	Sand	16	49	292.744	Sand

## 2.2 Classification Results

TabPFN is applied as an in-context classifier: the 16 training samples are provided as context, and the model predicts the class probability for each test sample without any gradient-based fine-tuning or hyperparameter tuning. On this test split, all 16 test samples were correctly classified (accuracy = 1.00, ROC-AUC = 1.00). Rather than focusing on this accuracy result alone, the following analysis examines the model’s predicted probability surface to assess the physical interpretability of the learned decision boundary.

Figure 2 shows the predicted probability of Sand,  $P(\text{Sand})$ , over the  $N$ – $V_s$  feature space. The model assigns high-confidence predictions near the training samples: the deep blue region coincides with

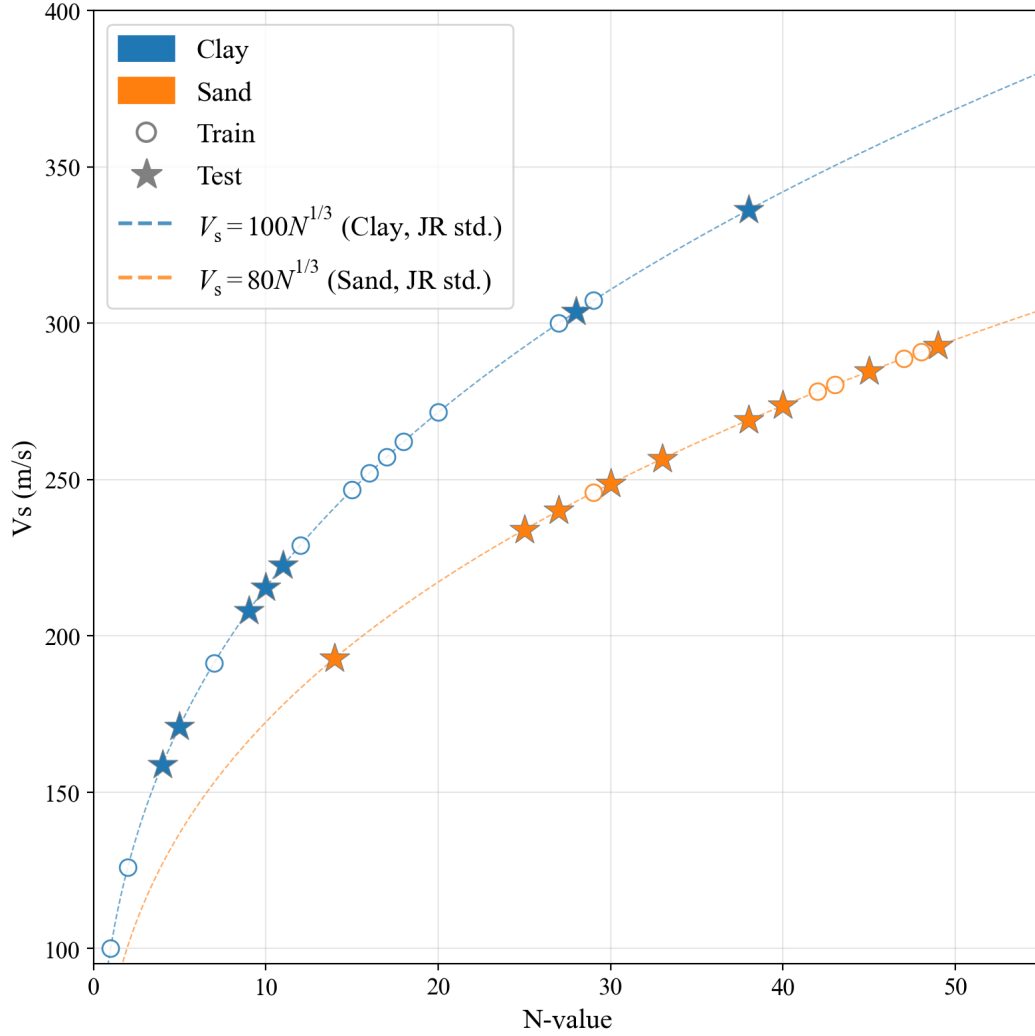


Figure 1: Scatter plots of training (circles) and test (stars) data in the  $N - V_s$  space, coloured by soil class (Clay: blue, Sand: orange). Training and test sets each contain 16 samples. Reference curves  $V_s = 100N^{1/3}$  and  $V_s = 80N^{1/3}$  from the Japanese railway seismic design standard [11] are overlaid; Clay samples follow the upper curve and Sand samples the lower curve.

the cluster of Clay training points, and the deep orange region aligns with the Sand training points at  $N \geq 29$ . The decision boundary tracks the lower envelope of the Clay  $N-V_s$  trend, implying that the model has learned the joint relationship between penetration resistance and shear-wave velocity characteristic of each soil class. In physically atypical corners—high  $N$  combined with very low  $V_s$  (lower right of the plot), and very low  $N$  combined with high  $V_s$  (upper left)—the predicted probability shifts toward  $P \approx 0.5$ , indicating that the model appropriately reduces its confidence when extrapolating far from training data. The shape of the boundary is physically interpretable: granular soils (Sand) are characterised by high penetration resistance ( $N$ ), whereas fine-grained soils (Clay) tend to exhibit higher shear-wave velocity relative to their penetration resistance—consistent with empirical  $N-V_s$  relationships that place Clay above Sand in the  $N-V_s$  space. One exception is the low- $N$ , low- $V_s$  corner, where the predicted probability shifts toward Sand despite Clay training samples being present in that region (Figure 2). This arises because no Sand training samples exist in this part of the feature space; without contrasting examples, the model cannot infer the correct class boundary, and the prediction diverges from physically expected behaviour. The dashed reference curves ( $V_s = 100N^{1/3}$  for Clay and  $V_s = 80N^{1/3}$  from the railway design standard) confirm that the

$P = 0.5$  boundary aligns well with engineering practice across most of the domain, but deviates in data-sparse regions.

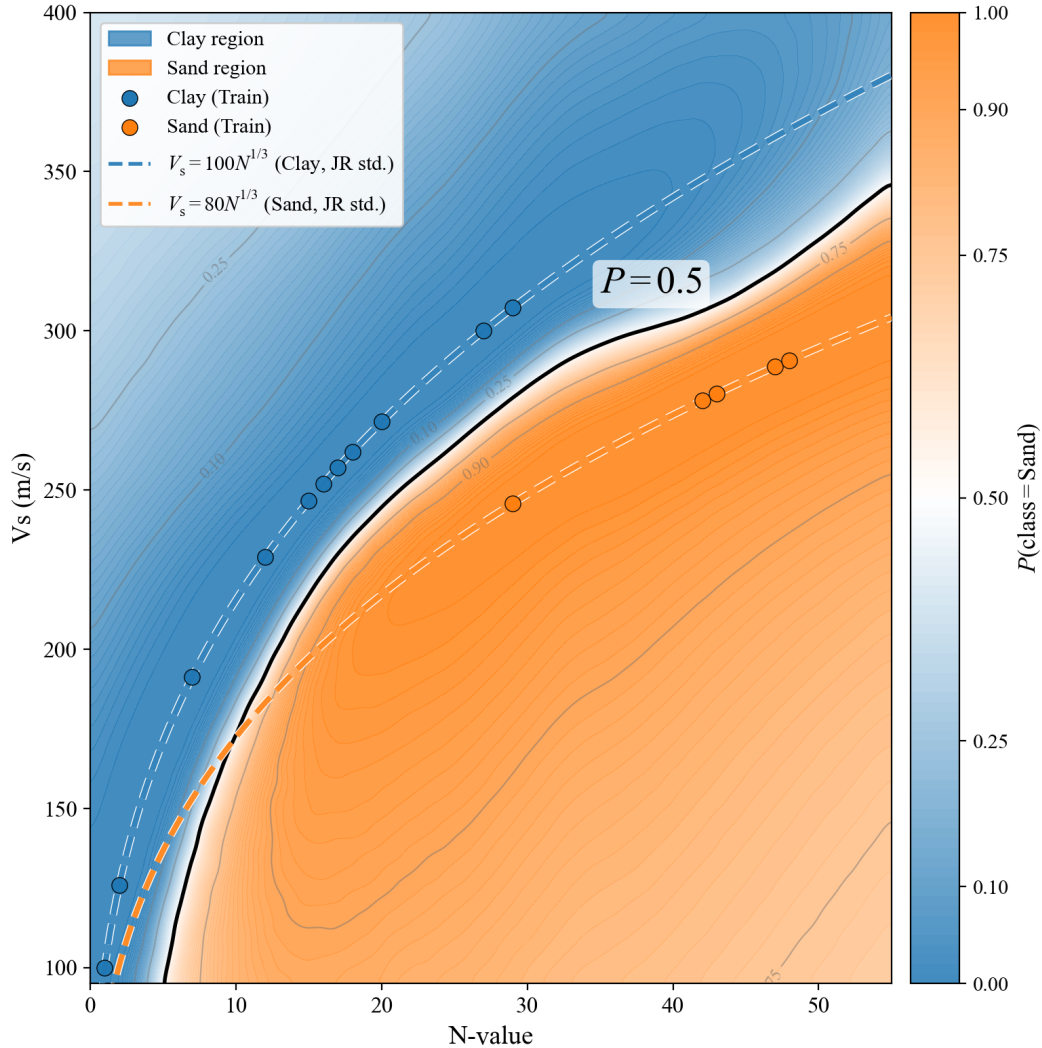


Figure 2: Predicted probability of Sand class  $P(\text{Sand})$  over the  $N - V_s$  domain, with the training samples overlaid (circles). The bold contour marks the decision boundary at  $P(\text{Sand}) = 0.5$ ; grey contours indicate the 0.1, 0.25, 0.75, and 0.9 levels.

### 2.3 Embedding Analysis

A distinctive property of TabPFN as a foundation model is its contextually enriched internal representations, made accessible through the `tabpfn-extensions` library. TabPFN encodes each sample into a high-dimensional latent vector (embedding) via multi-head attention over the entire training context, so that each vector captures not only the sample’s own feature values but also how it relates to every other sample in the dataset. This contextual encoding—in which each embedding is shaped by the full training set rather than derived from a single sample in isolation—enables a form of *relational reasoning* that is qualitatively different from the internal representations of conventional task-specific models. Because these embedding vectors are produced by attention-based aggregation, their pairwise cosine similarities provide a natural and interpretable measure of inter-sample affinity in the model’s learned representation space. Visualising these similarities therefore provides a window into the model’s internal grouping structure without requiring any external probing classifier or dimensionality reduction.

Figure 3 shows the cosine-similarity matrix between test embeddings (columns, No. 1–16) and training embeddings (rows, No. 1–16), ordered by soil class (Clay first, then Sand) and ascending  $N$ -value within each class, consistent with the sample numbering in Table 1.

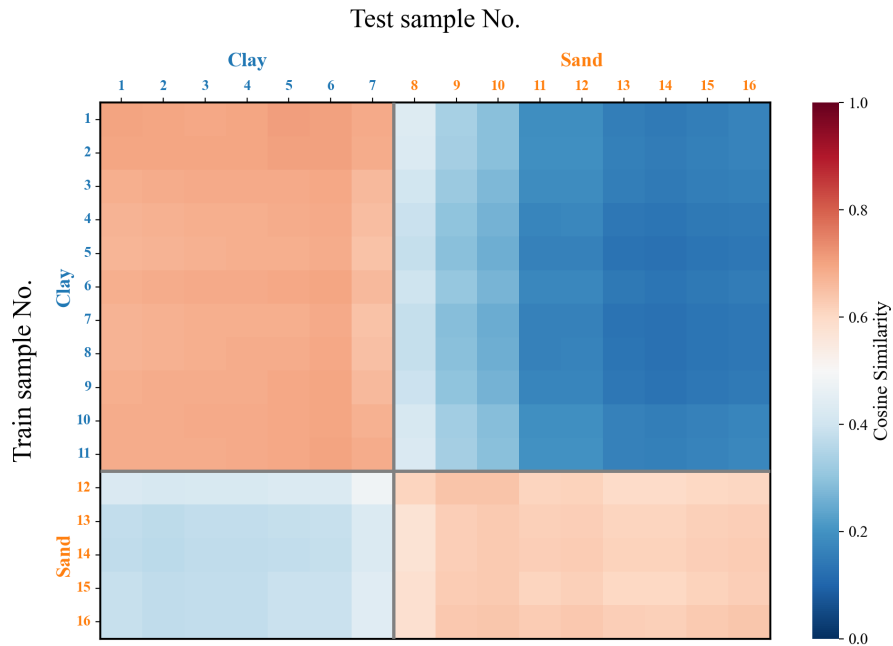


Figure 3: Cosine similarity heatmap of TabPFN embeddings between test and training samples (axis labels correspond to Table 1 No.). The block-diagonal structure confirms that the model internally separates Clay and Sand samples. Test sample No. 8 (first Sand test sample;  $N = 14$ ,  $V_s = 193$  m/s) shows visibly lower similarity with the training Sand block, reflecting the model’s reduced confidence at this out-of-distribution boundary point.

The block-diagonal structure in Figure 3 clearly demonstrates that Clay samples cluster together and Sand samples cluster together in the learned embedding space, confirming that TabPFN has captured the Clay–Sand distinction in its internal representation even without explicit soil-type label supervision at the embedding level.

A noteworthy exception is Test sample No. 8 (the first Sand test sample;  $N = 14$ ,  $V_s = 193$  m/s), whose column in the heatmap exhibits a conspicuously lower cosine similarity with the training Sand block compared to other Sand test samples, producing near-neutral values across both soil-class blocks. Test No. 8 falls at  $N = 14$ , entirely outside the range of Sand training data ( $N \geq 29$ ), and its  $(N, V_s)$  coordinates overlap with the Clay training distribution. The model thus lacks a clear analogy in its training context for this sample, and the embedding-level ambiguity is a direct reflection of that geometric uncertainty. Importantly, this ambiguity is not visible in the predicted probability surface (Figure 2): Test No. 8 receives a similarly high  $P(\text{Sand})$  as other Sand test samples, and the classification difficulty goes undetected from the probability output alone. It is only through the cosine-similarity heatmap in Figure 3 that the model’s internal uncertainty about this boundary sample becomes quantitatively apparent—illustrating the diagnostic value of embedding analysis as a complement to probability-based classification.

From a geotechnical engineering perspective, this embedding analysis offers practical capabilities beyond classification accuracy alone. The cosine-similarity matrix serves as a quantitative measure of how well a new borehole sample is “covered” by the training data: samples with uniformly low similarity across all training samples may represent out-of-distribution conditions that warrant additional field investigation before decisions are made. The analysis can also identify anomalous samples—those whose embedding profile is inconsistent with any established cluster—and assess the representativeness of a candidate training dataset before field measurements are finalised. In data-scarce geotechnical practice, where training sets frequently consist of only tens of samples, such a built-in coverage diagnostic is of direct operational value.

This example demonstrates how TabPFN embeddings can provide additional interpretability beyond classification accuracy by revealing the internal structure of the dataset—offering a data-driven analogue to the similarity-based site characterisation methods established in the geotechnical literature [14, 15]. These results suggest that embedding representations derived from foundation models may serve as a quantitative basis for inter-site similarity assessment, complementing conventional index-based approaches in geotechnical practice.

### 3 Regression Problem: Interpretable Multivariate Inference

This section demonstrates how TabPFN and its extensions can support interpretable multivariate inference for geotechnical parameters. The iterative inference procedure and posterior distributions (Sections 3.2–3.3) rely on TabPFN’s native prediction capabilities, whereas SHAP-based feature importance analysis (Section 3.4) uses the permutation explainer provided by `tabpfn-extensions`.

#### 3.1 Problem Setting

We address benchmark problem BM/AirportSoilProperties/2/2025 [7], which involves the prediction of five mechanical parameters—undrained shear strength  $s_u$ , undrained secant modulus  $E_u$ , preconsolidation pressure  $\sigma'_p$ , compression index  $C_c$ , and coefficient of consolidation  $C_v$ —from six index properties: saturation degree  $S_r$ , unit weight  $\gamma_t$ , void ratio  $e$ , liquid limit  $LL$ , plastic limit  $PL$ , and natural water content  $w$ . The dataset comprises  $n_{\text{train}} = 2,766$  training samples and  $n_{\text{test}} = 20$  test samples, each representing test results obtained from a soil specimen sampled at a given depth of a borehole. The training samples contain no missing values; for the test samples, some mechanical parameters may already be observed while others are treated as missing targets to be predicted. Unlike Saito et al. [12], who restricted predictions to the six index properties as the sole feature set ( $d = 6$ ), the present study includes the mechanical parameters themselves as additional features ( $d = 10$ ), enabling inter-parameter information to be exploited during inference.

#### 3.2 Iterative Inference Procedure

To leverage the cross-parameter dependencies among the five mechanical parameters, we adopt an iterated conditional mean procedure—a deterministic analogue of Gibbs sampling in which each mechanical parameter is sequentially updated using the posterior mean rather than a random draw from the conditional distribution. The procedure is as follows:

1. **Initialisation.** For each test sample, mechanical parameters that are already observed are kept at their measured values; the remaining (missing) parameters are initialised with the training-set mean. The six index properties ( $S_r$ ,  $\gamma_t$ ,  $e$ ,  $LL$ ,  $PL$ ,  $w$ ) are treated as fixed observed features ( $d_{\text{fixed}} = 6$ ).
2. **Iterative update** (repeat for  $k = 1, \dots, 10$ ). For each target parameter  $j \in \{s_u, E_u, \sigma'_p, C_c, C_v\}$ :
  - (a) Construct the feature matrix from the six index properties plus the current estimates of the four non-target mechanical parameters ( $d = 10$ ).
  - (b) Fit TabPFN on the training data and predict the full posterior distribution of parameter  $j$  for all test samples.
  - (c) For test samples in which parameter  $j$  is missing, update its estimate with the posterior mean; observed values are held fixed.
3. **Output.** Retain the posterior distributions from the final iteration for uncertainty quantification and downstream analysis.

This pattern-agnostic strategy estimates each parameter column-wise for all test samples uniformly, without conditioning on the specific combination of observed and missing parameters for each sample—in contrast to Saito et al. [12], who fitted separate models for each distinct missing-data pattern.

Figure 4 shows the normalised RMSE (relative to iteration 1) for each mechanical parameter across iterations. Four of the five parameters— $s_u$ ,  $E_u$ ,  $\sigma'_p$ , and  $C_c$ —exhibit monotonic decreases, with  $s_u$  showing the largest relative improvement ( $\sim 18\%$  reduction), confirming that the iterative scheme

effectively propagates inter-parameter information. In contrast,  $C_v$  remains at or slightly above the initial RMSE throughout the iterations (Table 2: 73.51  $\rightarrow$  74.42), indicating that conditioning on other mechanical parameters does not improve—and marginally degrades—its prediction. This is attributable to the high intrinsic variability of  $C_v$ , which limits the useful information that correlated parameters can contribute. Although the number of iterations ( $K = 10$ ) was set without a formal convergence criterion, the consistent improvement observed for four parameters demonstrates the potential of iterative conditioning to enhance multivariate geotechnical inference; establishing optimal stopping rules remains a topic for future investigation.

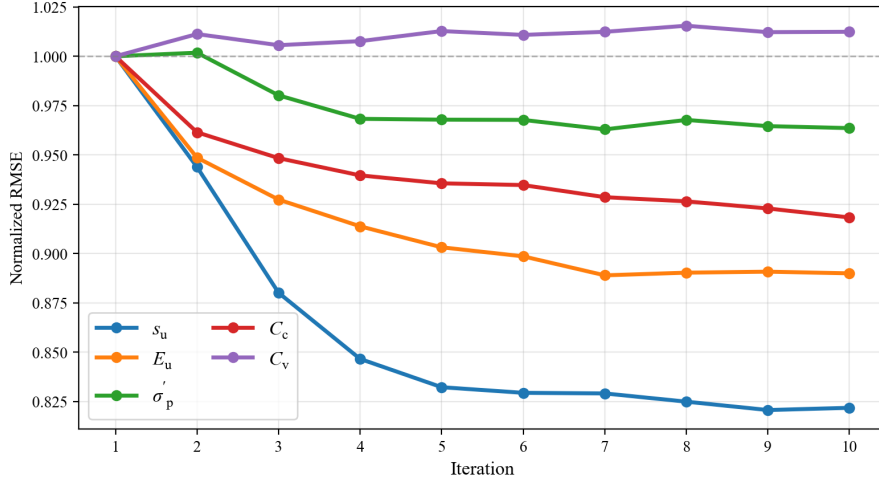


Figure 4: Normalised RMSE (RMSE / RMSE at iteration 1) per iteration for each mechanical parameter. Values below 1.0 indicate improvement over the initial estimate.

Table 2 summarises the absolute RMSE values at iteration 1 and iteration 10. The improvement is most pronounced for  $s_u$  and  $E_u$ , while  $C_c$  achieves a modest but consistent reduction.

Table 2: RMSE at iteration 1 and iteration 10 for each mechanical parameter.

Parameter	RMSE (iter. 1)	RMSE (iter. 10)
$s_u$ (kN/m <sup>2</sup> )	13.88	11.41
$E_u$ (kN/m <sup>2</sup> )	3254	2896
$\sigma'_p$ (kN/m <sup>2</sup> )	32.40	31.23
$C_c$ (—)	0.112	0.102
$C_v$ (m <sup>2</sup> /s)	73.51	74.42

### 3.3 Posterior Distributions

Figure 5 displays violin plots of the posterior distributions at the final iteration (iteration 10) for all five mechanical parameters across test samples. Each violin represents the full predictive distribution for a single sample; the black bar indicates the median, and the yellow circle the true value. Black filled circles indicate samples for which the parameter was already observed (not missing) and therefore not predicted.

The posterior widths reflect parameter-specific predictability:  $C_c$  and  $\sigma'_p$  show relatively narrow distributions, while  $C_v$  exhibits broad posteriors consistent with its high intrinsic variability. In most samples, the true value lies within the high-density region of the posterior, suggesting that the model’s uncertainty estimates are physically plausible, though formal calibration analysis is deferred to future work. One practical caveat is that TabPFN’s discretised output representation can occasionally assign non-negligible probability mass to extreme values, resulting in elongated distribution tails; the median is therefore the more reliable point estimate in such cases.

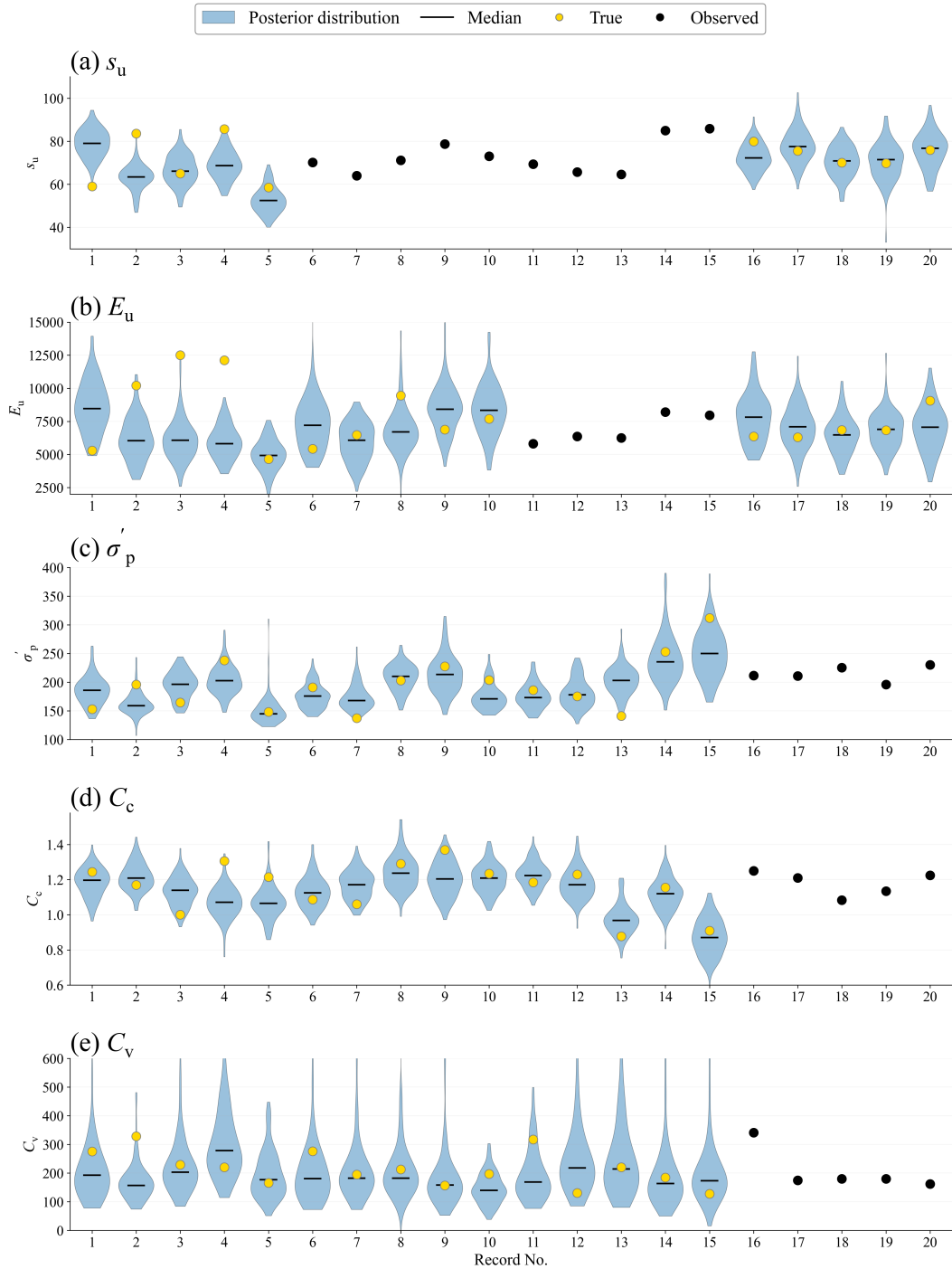


Figure 5: Posterior distributions at iteration 10 for all five mechanical parameters across test samples. Violin width represents the probability density; black bar = median; yellow circle = true value; black filled circle = observed value (parameter was not missing for that sample and therefore not predicted).

### 3.4 Feature Importance via SHAP

A key objective of this section is to reveal the inter-parameter dependency structure learned by TabPFN through the iterative inference procedure. Prior Bayesian approaches to geotechnical multivariate inference—such as hierarchical Bayesian models [3, 17]—characterise inter-parameter correlations explicitly through a probabilistic model. SHAP-based attribution provides a complementary, model-agnostic perspective: by quantifying each feature’s marginal contribution to individual predictions, it allows the dependency structure to be read directly from the trained model without assuming a parametric correlation form. To identify which input features most strongly influence each mechanical parameter prediction, we computed SHAP values [5] using the permutation explainer provided by `tabpfn-extensions`, applied to the final-iteration TabPFN model. Figure 6 shows the mean absolute SHAP value for each feature grouped by parameter, and Figure 7 plots the SHAP value of the most influential index property against its feature value for each target parameter.

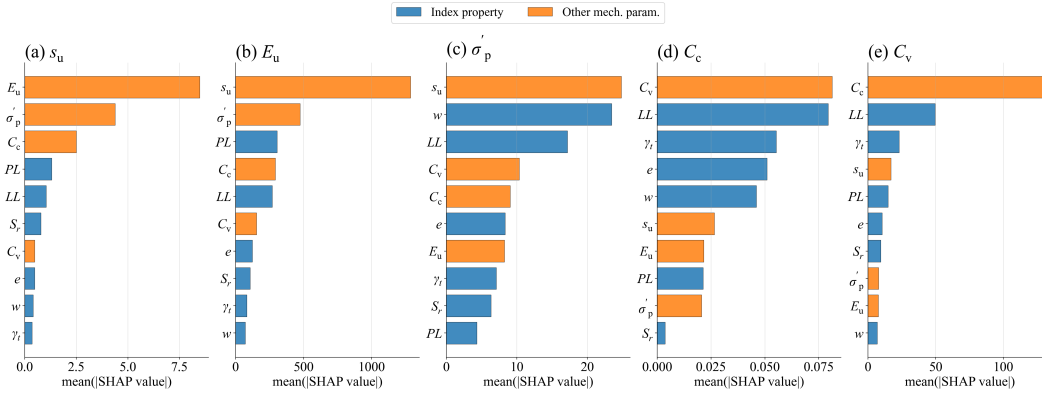


Figure 6: Mean absolute SHAP values for each input feature across all test samples, shown separately for each mechanical parameter. Blue bars: index properties; orange bars: other mechanical parameters used as features in the iterative imputation scheme.

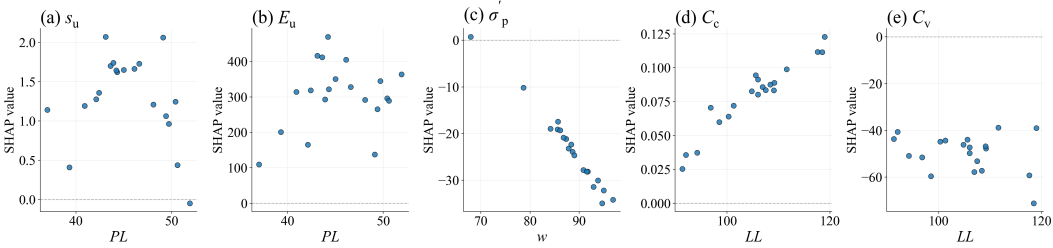


Figure 7: SHAP value of the most influential index property versus its feature value, shown for each mechanical parameter: (a)  $s_u$  and (b)  $E_u$  versus plastic limit  $PL$ ; (c)  $\sigma'_p$  versus water content  $w$ ; (d)  $C_c$  and (e)  $C_v$  versus liquid limit  $LL$ . Positive SHAP values indicate that the feature increases the predicted value; negative values indicate a decrease.

The results reveal two distinct regimes of feature dominance. For  $C_c$ , the coefficient of consolidation  $C_v$  (another mechanical parameter) is the single most influential predictor, followed by the liquid limit  $LL$ . The prominence of  $LL$  is physically consistent with the classical empirical correlation  $C_c \approx 0.007(LL - 10)$  [16], and the scatter plot (Figure 7d) confirms a positive monotonic relationship: samples with higher  $LL$  receive larger positive SHAP contributions toward  $C_c$ . Similarly,  $C_v$  is most strongly influenced by  $C_c$ , followed by  $LL$  and unit weight  $\gamma_t$ , reflecting the physical dependence of consolidation rate on compressibility; the scatter plot (Figure 7e) shows that higher  $LL$  suppresses the predicted  $C_v$ , consistent with the inverse relationship between plasticity and drainage rate in fine-grained soils. In contrast, for  $s_u$ ,  $E_u$ , and  $\sigma'_p$ , other mechanical parameters dominate over index properties:  $E_u$  is the strongest predictor of  $s_u$ , and  $s_u$  reciprocally dominates  $E_u$ . Correspondingly, the scatter plots for  $s_u$  and  $E_u$  against their top-ranked index property ( $PL$ ; Figure 7a,b) show relatively diffuse patterns, consistent with the subordinate role of index properties in predicting

these strength and stiffness parameters. For  $\sigma'_p$ , both  $s_u$  and water content  $w$  are nearly co-equal top predictors, with  $LL$  also ranking highly; the scatter plot (Figure 7c) reveals a strong negative dependence of the  $w$ -based SHAP contribution on  $w$  itself, meaning that samples with high natural water content are predicted to have lower preconsolidation pressure—consistent with the well-known inverse relationship between  $w$  and  $\sigma'_p$  in normally to lightly overconsolidated clays. This cross-parameter influence reflects the iterative imputation scheme, in which the model leverages progressively refined estimates of correlated parameters to improve prediction accuracy.

## 4 Discussion

The results demonstrate that TabPFN and its extensions provide three complementary interpretability tools beyond raw accuracy: embedding similarity (via `tabpfn-extensions`), posterior uncertainty (via TabPFN’s native quantised output), and SHAP-based feature importance (via `tabpfn-extensions`). Across both the classification and regression tasks, the model’s outputs align with established geotechnical knowledge without domain-specific fine-tuning, relying solely on in-context learning from the small training set.

**Embedding-based interpretability.** The cosine-similarity heatmap (Figure 3) reveals that TabPFN organises samples by soil type in its internal representation space, even though no explicit soil-type label is used during the classification inference. This supports the use of embedding analysis as a data-quality check: new borehole samples that do not cluster with established soil types may warrant additional investigation.

**Posterior uncertainty.** The full posterior distributions obtained via TabPFN’s quantised output (Figure 5) provide uncertainty estimates that are immediately usable in reliability-based design. Unlike point-estimate regressors, this approach quantifies prediction confidence sample-by-sample, enabling engineers to flag highly uncertain predictions for follow-up testing. Notably,  $C_v$ —which has high intrinsic variability and is difficult to measure reliably—exhibits the broadest posteriors, while  $C_c$  and  $\sigma'_p$  show comparatively narrow distributions; this ordering is physically reasonable and suggests that the model’s uncertainty estimates reflect true parameter predictability rather than arbitrary numerical dispersion.

**Feature importance and inter-parameter dependency.** SHAP-based importance (Figures 6 and 7) reveals a physically interpretable dual structure in the inter-parameter dependency learned by the model. For consolidation parameters, mutual cross-parameter influence and index properties both play roles:  $C_v$  leads for  $C_c$  with  $LL$  as the top index property (consistent with the Skempton correlation), while  $C_c$  dominates  $C_v$  with  $LL$  suppressing consolidation rate in high-plasticity soils. For strength and stiffness parameters ( $s_u$ ,  $E_u$ ,  $\sigma'_p$ ), other mechanical parameters outrank index properties, with  $w$  emerging as a physically meaningful co-dominant predictor of  $\sigma'_p$ , indicating that the iterative imputation scheme efficiently propagates information across correlated targets. This two-regime structure—index-property and cross-parameter influence for compressibility, cross-parameter dominance for strength—is consistent with established geotechnical knowledge and supports the physical plausibility of the model’s learned representations. Compared with hierarchical Bayesian approaches [3, 17], which characterise inter-parameter correlations through explicitly specified probabilistic models, the SHAP-based analysis provides a complementary and more granular view: it quantifies asymmetric, nonlinear dependencies between individual parameters at the sample level, without requiring a parametric correlation structure to be assumed in advance.

**Comparison with existing approaches.** Table 3 provides a qualitative comparison of the interpretability and extensibility capabilities offered by three representative modelling frameworks applied to geotechnical parameter inference: hierarchical Bayesian models (HBM) [3, 17] and conventional machine-learning methods such as random forests and recurrent neural networks, which have been applied to geotechnical parameter prediction and site characterisation [6, 18], alongside TabPFN with extensions (this study). The comparison focuses not on predictive accuracy, which was benchmarked in our companion study [12], but on the range of post-prediction analysis tools available to the practitioner. HBM provides well-calibrated posterior distributions through an explicitly specified probabilistic model, but does not natively offer embedding-based similarity analysis or model-agnostic feature attribution. Conventional ML methods can be coupled with permutation-based SHAP, yet they

produce only point estimates unless additional techniques (e.g. quantile regression forests, Monte Carlo dropout) are employed, and lack a built-in embedding representation. TabPFN combines native posterior outputs, contextual embeddings, and SHAP attribution within a single framework, all without model retraining or hyperparameter tuning—offering a uniquely integrated toolkit for interpretable geotechnical inference.

Table 3: Qualitative comparison of interpretability and extensibility capabilities across modelling frameworks for geotechnical parameter inference.

Capability	HBM	Conv. ML <sup>†</sup>	TabPFN + Ext.
Posterior distribution	Yes (parametric)	No*	Yes (native)
Embedding similarity	No	No	Yes
SHAP feature importance	No	Yes	Yes
No retraining required	No	No	Yes
Correlation structure	Parametric	—	Non-parametric

<sup>†</sup>Conventional ML methods (e.g. random forests, RNN) [6, 18].

\*Requires additional techniques (e.g. quantile regression forests, Monte Carlo dropout).

**Limitations.** Several limitations should be acknowledged. As an in-context learner, TabPFN’s decision boundaries are governed entirely by the training samples provided at inference time; in regions of the feature space that lack training samples of one class, the model cannot infer a physically meaningful boundary and may extrapolate in an unintuitive direction. This is evident in the low- $N$ , low- $V_s$  region of Figure 2, where the absence of Sand training samples causes the model to predict Sand despite Clay being the physically expected class. Expanding or diversifying the training set to cover the full feature space would mitigate this behaviour. Additionally, the iterative imputation procedure used for the regression benchmark assumes that the model’s predictive distribution is well-calibrated at each iteration; systematic miscalibration could propagate errors across targets. Further validation on independent datasets from different geological settings is needed to confirm the generalisability of the approach.

## 5 Conclusion

We have demonstrated that TabPFN and its extensions provide a practical suite of interpretability tools—embedding analysis (via `tabpfn-extensions`), posterior distributions (via TabPFN’s native quantised output), and SHAP-based feature importance (via `tabpfn-extensions`)—that complement predictive accuracy in geotechnical engineering applications. For the soil classification task, cosine-similarity heatmaps of learned embeddings clearly separated Clay and Sand samples without any explicit soil-type supervision, demonstrating that the model captures physically meaningful soil structure through in-context learning alone. For the regression benchmark, iterative imputation improved predictions for four of five mechanical parameters, posterior distributions reflected physically reasonable parameter-specific uncertainty (e.g., broad posteriors for  $C_v$ , narrow for  $C_c$ ), and SHAP analysis recovered established geotechnical relationships such as the Skempton correlation and the inverse dependence of  $\sigma'_p$  on water content. These results position TabPFN as not merely a high-accuracy predictor, but a transparent and interpretable tool for AI-assisted site characterisation under data-scarce conditions, suggesting that foundation model-based inference may offer a new paradigm for data-driven geotechnical engineering. Future work includes domain-specific fine-tuning of the foundation model on large-scale geotechnical databases to develop a civil-engineering-specialised variant, as well as exploration of large language model (LLM) integration for natural-language explanation of predicted parameters and uncertainty estimates.

## Acknowledgments and Disclosure of Funding

This research was supported by JSPS KAKENHI Grant Numbers JP23H00195 and JP25KJ0619.

## References

- [1] Yongmin Cai, Kok-Kwang Phoon, Qiuqing Pan, and Wuzhang Luo. Modifying the tailored clustering enabled regionalization (TCER) framework for outlier site detection and inference efficiency. *Engineering Geology*, 335:107537, 2024. doi: 10.1016/j.enggeo.2024.107537.
- [2] Yongmin Cai, Kok-Kwang Phoon, Yu Otake, and Yu Wang. Efficient dictionary learning for constructing quasi-local transformation models. *Computers and Geotechnics*, 180:107072, 2025. doi: 10.1016/j.compgeo.2025.107072.
- [3] Jianye Ching, Stephen Wu, and Kok-Kwang Phoon. Constructing quasi-site-specific multivariate probability distribution using hierarchical Bayesian model. *Journal of Engineering Mechanics*, 147(10):04021069, 2021. doi: 10.1061/(ASCE)EM.1943-7889.0001964.
- [4] Noah Hollmann, Samuel Müller, Lennart Purucker, Arjun Krishnakumar, Max Thomas, Shi Bin Hoo, Eddie Bergman, and Frank Hutter. Accurate predictions on small data with a tabular foundation model. *Nature*, 637:319–326, 2025. doi: 10.1038/s41586-024-08328-6.
- [5] Scott M. Lundberg and Su-In Lee. A unified approach to interpreting model predictions. In *Advances in Neural Information Processing Systems 30*, pages 4765–4774, 2017. URL <https://proceedings.neurips.cc/paper/2017/hash/8a20a8621978632d76c43dfd28b67767-Abstract.html>.
- [6] Prajowal Manandhar, Tarek Abdoun, Mostafa E. Mobasher, and Waleed El-Sekelly. Predicting soil properties for the purpose of site characterization using advanced machine learning approaches. *Geodata and AI*, page 100054, 2026. doi: 10.1016/j.geoai.2026.100054.
- [7] Yu Otake, Jianye Ching, Taiga Saito, and Kotaro Asano. GEOAI benchmark problems BM/AirportSoilProperties/2/2025. *Geodata and AI*, 2:100012, 2025. doi: 10.1016/j.geoai.2025.100012.
- [8] Kok-Kwang Phoon, Jianye Ching, and Takayuki Shuku. Challenges in data-driven site characterization. *Georisk: Assessment and Management of Risk for Engineered Systems and Geohazards*, 16(1):114–126, 2022. doi: 10.1080/17499518.2021.1896005.
- [9] Kok-Kwang Phoon, Yongmin Cai, and Chong Tang. Geotechnical “facial recognition” challenge. *ASCE-ASME Journal of Risk and Uncertainty in Engineering Systems, Part A: Civil Engineering*, 11(3):03125001, 2025. doi: 10.1061/AJRUA6.RUENG-1553.
- [10] Prior Labs. tabpfn-extensions. <https://github.com/priorlabs/tabpfn-extensions>. Accessed: 2026-03-11.
- [11] Railway Technical Research Institute. *Design Standards for Railway Structures and Commentary: Seismic Design*. Maruzen Publishing, Tokyo, Japan, 2012. (In Japanese: Tetsudo Kozobutsu-to Sekkei Hyojun – Dokaisetsu: Taishin Sekkei, September 2012).
- [12] Taiga Saito, Yu Otake, and Stephen Wu. Applying a tabular foundation model to geotechnical site characterization. *Geodata and AI*, page 100040, 2025. doi: 10.1016/j.geoai.2025.100040.
- [13] Taiga Saito, Yu Otake, Stephen Wu, and Keisuke Yano. Exploring high-order multivariate geotechnical features using the minimum information dependence model. *Geodata and AI*, 2:100009, 2025. doi: 10.1016/j.geoai.2025.100009.
- [14] Atma Sharma, Jianye Ching, and Kok-Kwang Phoon. A hierarchical Bayesian similarity measure for geotechnical site retrieval. *Journal of Engineering Mechanics*, 148(9):04022045, 2022. doi: 10.1061/(ASCE)EM.1943-7889.0002145.
- [15] Atma Sharma, Jianye Ching, and Kok-Kwang Phoon. A spectral algorithm for quasi-regional geotechnical site clustering. *Computers and Geotechnics*, 163:105624, 2023. doi: 10.1016/j.compgeo.2023.105624.
- [16] A. W. Skempton. Notes on the compressibility of clays. *Quarterly Journal of the Geological Society*, 100:119–135, 1944.

- [17] Stephen Wu, Jianye Ching, and Kok-Kwang Phoon. Quasi-site-specific soil property prediction using a cluster-based hierarchical Bayesian model. *Structural Safety*, 99:102253, 2022. doi: 10.1016/j.strusafe.2022.102253.
- [18] Runhong Zhang, Chongzhi Wu, Anthony T. C. Goh, Thomas Böhlke, and Wengang Zhang. Estimation of diaphragm wall deflections for deep braced excavation in anisotropic clays using ensemble learning. *Geoscience Frontiers*, 12(1):365–373, 2021. doi: 10.1016/j.gsf.2020.03.003.